

Dislocation Majorana Bound States in Iron-based Superconductors

Lun-Hui Hu^{1,2} and Rui-Xing Zhang^{1,3,2,*}

¹*Department of Physics and Astronomy, The University of Tennessee, Knoxville, Tennessee 37996, USA*

²*Institute for Advanced Materials and Manufacturing,
The University of Tennessee, Knoxville, Tennessee 37920, USA*

³*Department of Materials Science and Engineering,
The University of Tennessee, Knoxville, Tennessee 37996, USA*

(Dated: September 20, 2022)

We show that lattice dislocations of topological iron-based superconductors such as $\text{FeTe}_{1-x}\text{Se}_x$ will intrinsically trap non-Abelian Majorana quasiparticles, in the absence of any external magnetic field. Our theory is motivated by the recent experimental observations of normal-state weak topology and surface magnetism that coexist with superconductivity in $\text{FeTe}_{1-x}\text{Se}_x$, the combination of which naturally achieves an emergent second-order topological superconductivity in a two-dimensional subsystem spanned by screw or edge dislocations. This exemplifies a new *embedded* higher-order topological phase in class D, where Majorana zero modes appear around the “corners” of a low-dimensional embedded subsystem, instead of those of the full crystal. A nested domain wall theory is developed to understand the origin of these defect Majorana zero modes. When the surface magnetism is absent, we further find that s_{\pm} pairing symmetry itself is capable of inducing a different type of class-DIII embedded higher-order topology with defect-bound Majorana Kramers pairs. We also provide detailed discussions on the real-world material candidates for our proposals, including $\text{FeTe}_{1-x}\text{Se}_x$, LiFeAs , $\beta\text{-PdBi}_2$, and heterostructures of bismuth, etc. Our work establishes lattice defects as a new venue to achieve high-temperature topological quantum information processing.

I. INTRODUCTION

Crystals of quantum materials are rarely perfect in the real world. While it appears natural to always suppress lattice disorders and pursue crystals of a higher purity, defectiveness in topological quantum materials often binds exotic massless quasiparticles that hold great promise for future electronics. A prototypical example is the famous Jackiw-Rebbi problem [1] and its condensed matter realization in polyacetylene [2], where zero-energy fermionic modes are trapped by the domain wall defects of a one-dimensional (1D) dimerized atomic chain. Since then, gapless electronic or Majorana zero modes have been established in lattice or order-parameter defects of various topological phases, including weak and crystalline topological insulators (TIs) [3–7], topological superconductors (TSCs) [8–17], and topological semimetals [18, 19], etc. For example, locally irremovable lattice topological defects such as screw/edge dislocations can trap 1D helical bound states in 3D weak TIs, providing an intriguing bridge between lattice and electronic topologies. Experimental evidence for dislocation-trapped electronic modes has been reported in $\text{Bi}_{1-x}\text{Sb}_x$ [20] and bismuth [21], both of which are known to be weak TI candidates. Similar phenomena, if exist in superconductors (SC), would lead to a new mechanism of enabling Majorana modes. However, we are not aware of any realistic superconducting system that has been theoretically proposed or experimentally supported to feature Majorana dislocation-bound states.

Recent years have also witnessed a Majorana revolution in the high- T_c topological iron-based superconductors (tFeSCs), including $\text{FeTe}_{1-x}\text{Se}_x$ [22–24], $(\text{Li,Fe})\text{OHFeSe}$ [25], LiFeAs [26–28], etc. Notably, the topology of tFeSCs only lies in their normal states [29], that a band inversion at the Z point generates both a nontrivial \mathbb{Z}_2 electronic band topology and a helical Dirac surface state [30, 31]. Below the critical temperature T_c , a nodeless pairing gap is developed for both bulk and surface states, wiping out all normal-state topological physics around the Fermi energy. Despite the bulk-state triviality, striking evidence of Majorana signals has been extensively reported in superconducting vortices [22–28], atomic vacancies [32], and magnetic adatoms [33, 34]. While the vortex Majorana signals in tFeSCs are usually believed to arise from the Fu-Kane mechanism [35–37], origins of the vacancy/impurity-related zero-bias peaks are still under debate [38–43]. Noting that vacancies and add-on impurities are both locally removable and point-like, one may also wonder if extended irremovable lattice defects such as dislocations or disclinations could invoke any interesting *field-free* topological physics in tFeSCs.

Our main finding in this work is that screw or edge dislocations can naturally bind 0D Majorana zero modes in tFeSCs and similar superconducting systems, in the absence of any external magnetic field. Noting that a pair of dislocations, as well as the 2D “cutting plane” attached to them, can be viewed as an effective 2D subsystem embedded in a 3D crystal, the four dislocation Majorana bound states (dMBSs) manifest as “corner” Majorana modes for this 2D subsystem, one at each corner. Therefore, our mechanism exemplifies an unprecedented Majorana mechanism that is based on the second-order topology of 2D subsystems, which is in sharp contrast with

* ruixing@utk.edu

earlier proposals on vortex/vacancy Majorana modes enabled by the first-order topology for 1D subsystems (i.e., vortex/vacancy lines). We thus dub this new phase “embedded second-order topological phase” (ET₂).

ET₂ in tFeSCs is completely driven by the normal-state topology [30, 31], screw dislocations [44], and surface magnetism \mathbf{M} that coexists with superconductivity [45–48], all of which have been experimentally observed in FeTe_{1-x}Se_x. In particular, we show that dMBSs emerge once the dislocation Burgers vector $\mathbf{b} = (b_x, b_y, b_z)$ satisfies $b_z \equiv 1 \pmod{2}$, as a result of nested mass domains for surface Dirac fermions. Remarkably, this ET₂ condition is a natural outcome of a less recognized *weak* topological index $\nu = (0, 0, 1)$ of tFeSCs. Therefore, our theory is directly applicable to other weak-index-carrying superconducting topological materials, such as β -Bi₂Pd [49]. We further discuss the impact of s_{\pm} -wave pairing symmetry on our recipe, and find it capable of inducing a new type of class DIII ET₂ with dislocation Majorana Kramers pairs (dMKPs), in the absence of any surface magnetism. Promising real-world material candidates and experimental signatures are also discussed.

II. DISLOCATION MAJORANA BOUND STATES

We start by deriving the key result in our work, the recipe for dMBSs in tFeSCs, with the help of a nested domain wall construction approach. We then proceed to discuss boundary conditions of dislocation-induced cutting plane and find that a 0D dMBS can be “inflated” to a 1D “hinge” chiral Majorana fermion under certain circumstances. Nonetheless, each corner of the cutting plane will always host a single zero-energy mode. This directly leads to the concept of embedded higher-order topological phase ET₂.

A. Recipe for dMBSs

Let us first provide some motivations for our recipe. To trap a 0D bound state in a 3D system, one can start from a 3D gapless quasiparticle (e.g. a massless Dirac fermion) and further constrain its degrees of freedom (d.o.f.) in all three spatial directions. This “dimensional reduction” procedure can be feasibly achieved by decorating the Dirac fermion with a hierarchical set of \mathbb{Z}_2 mass domains, with each domain effectively reducing the dimension of gapless state by one. For example, the 2D gapless surface of a 3D TI can be viewed as a domain wall bound state for a 3D massive Dirac fermion, with the TI bulk and the outside vacuum carrying opposite Dirac masses, respectively. A second SC/magnetism domain for the 2D surface Dirac fermion further reduces the gapless d.o.f. to 1D, i.e., leading to a 1D chiral Majorana domain-wall mode [50, 51]. To eventually achieve a 0D Majorana mode, it clearly requires a third \mathbb{Z}_2 -type

mass domain wall. We will show that, under certain circumstances, lattice domains introduced by screw/edge dislocations can serve as mass domains and thus contribute the last piece of the jigsaw puzzle. This approach is thus dubbed a *nested domain wall* construction for defect MBSs.

Another key motivation is from the material side. Recent experimental breakthroughs have revealed hidden topological Dirac surface states for several high-T_c iron-based SCs [30, 31]. Among these tFeSC candidates, FeTe_{1-x}Se_x is of particular interest to us, as it additionally harbors surface ferromagnetism that coexists with bulk superconductivity below its superconducting T_c ~ 14.5 K [45–48]. Furthermore, screw dislocations for FeTe_{1-x}Se_x can be generated in a highly controllable manner during the growth process [44]. Therefore, it is natural to expect FeTe_{1-x}Se_x to be a wonderful playground for studying a new lattice topological defect-based Majorana platform in the absence of any external magnetic field. And a possible recipe for Majorana bound states will be extremely helpful to diagnose the topological situation here.

We now derive the topological condition of defect MBSs for tFeSCs. Our starting point is a 3D TRI TI with bulk isotropic s -wave spin-singlet superconductivity. The normal-state topology is indicated by a strong \mathbb{Z}_2 topological index ν_0 and a set of weak \mathbb{Z}_2 indices $\nu = (\nu_1, \nu_2, \nu_3)$ [35]. In particular, $\nu_0 = 0$ ($\nu_0 = 1$) dictates an even (odd) number of Dirac surface states, while the values of weak indices $\nu_{1,2,3}$ decide the momentum-space locations of the surface states. The bulk s -wave SC, however, necessarily spoils the normal-state topology by introducing an isotropic SC gap δ_{SC} to all Dirac surfaces through a “self-proximity” effect. Motivated by FeTe_{1-x}Se_x, we further introduce surface magnetism δ_{M} to both top and bottom (001) surfaces of our TI system. The explicit type of magnetism is flexible as long as it can act as a mass term for Dirac surface state and further competes with the surface SC. Since the side surfaces are magnetism-free, when

$$|\delta_{\text{M}}| > |\delta_{\text{SC}}|, \quad (1)$$

a SC/magnetism domain emerges around the edges between top/bottom and side surfaces. This condition thus generates a 1D chiral Majorana mode around both top and bottom surfaces, i.e., a chiral Majorana hinge mode. We emphasize that the chiral Majorana hinge mode here is a result of 2D surface topology alone, that the top and bottom surfaces both feature a BdG Chern number of $|\mathcal{C}| = 1$, as will be discussed in Sec. III B. The 3D bulk topology will not be altered and thus remains trivial throughout the surface magnetism decoration.

Our last ingredient, the lattice dislocations, is intuitively a “gluing fault” when combining two identical copies of our setup. For example, as schematically shown in Fig. 1 (a), the screw dislocations are formed when the left parts of the two crystals are combined perfectly, while the right parts mismatch with each other by a displace-

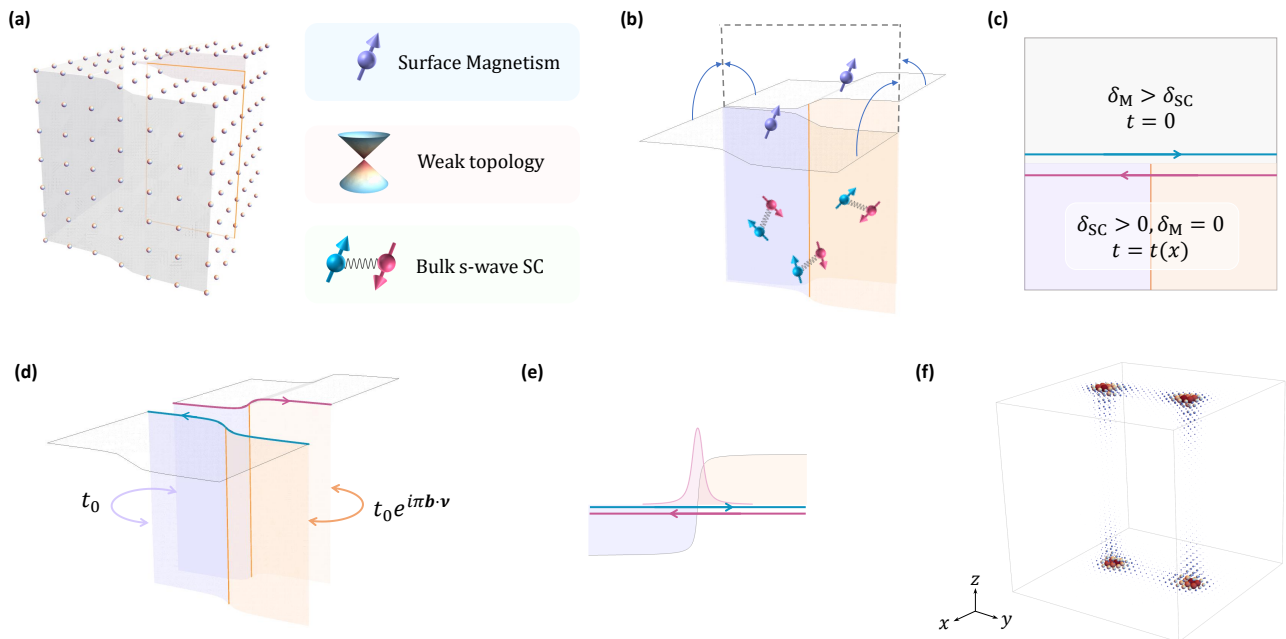


FIG. 1. Nested domain wall theory for class-D ET_2 . (a) shows a single screw dislocation with a Burgers vector $\mathbf{b} = (0, 0, 1)$ along with other key ingredients for ET_2 : weak electronic topology, bulk SC, and surface magnetism. In (b), we cut the crystal in halves following the orange cutting plane in (a), which leads to two disjoint magnetism-gapped top surfaces and two SC-gapped side surfaces. Further folding the top surfaces following the trajectory arrows leads to the “bilayer” configurations of Dirac surface states in (c). The competition between magnetism (M) and SC leads to a pair of counterpropagating 1D Majorana modes once $\delta_M > \delta_{SC}$. In (d), we glue everything together to restore the crystal, and the introduction of a dislocation decorates the intersurface hopping between Dirac particles on the orange cutting plane with a phase factor of $e^{i\pi \mathbf{b} \cdot \boldsymbol{\nu}}$. This gaps out the Majorana modes in a nontrivial way shown in (e), which can be mapped to a 1D Jackiw-Rebbi domain wall problem and results in a localized Majorana zero mode at the surface dislocation core. We carry out a numerical simulation of a pair of screw dislocations for $FeTe_{1-x}Se_x$ on a $28 \times 28 \times 28$ lattice. Four zero-energy modes are found and their spatial wavefunctions are found to be localized around each dislocation core, as shown in (f).

ment vector $\mathbf{b}=(0,0,1)$, i.e., the Burgers vector. While a screw or an edge dislocation appears one-dimensional, it must be attached to a 2D *cutting plane* \mathcal{P}_c that only terminates at either another dislocation to form a dislocation dipole or the crystal boundary. Example of a cutting plane is highlighted by the orange line in Fig. 1 (a).

To explore the fate of chiral Majorana hinge modes during the gluing process, it is helpful to fold the top surfaces of the two to-be-glued crystals as shown in Fig. 1 (b). Then the previous interfacial problem is now mapped to a 2D bilayer system in the y - z plane, with each layer hosting a TI surface state. Distribution of δ_M and δ_{SC} are shown in Fig. 3 (c). The domain wall will bind a pair of counterpropagating chiral Majorana modes as denoted by the green and red arrows in Fig. 1 (c). Combining the two crystals is equivalent to introducing an interlayer coupling t for only the bottom parts of the bilayer, i.e., the previous side surfaces, which will also couple the oppositely propagating Majorana modes and gap them out. However, the interlayer mass term for the Majorana fermions will obtain a phase factor $e^{i\pi \mathbf{b} \cdot \boldsymbol{\nu}}$, following the side Dirac surface states [3]. In the presence of a lattice dislocation, the cutting plane [i.e., orange region in Fig. 1 (c)] features a finite Burgers vector \mathbf{b} , while the

purple region has a zero Burgers vector because of the perfect lattice matching. Assuming the dislocation at $y = 0$, we have the mass term

$$t(y) = \begin{cases} t_0 & y < 0, \\ t_0 e^{i\pi \mathbf{b} \cdot \boldsymbol{\nu}} & y > 0. \end{cases} \quad (2)$$

Crucially, when

$$\mathbf{b} \cdot \boldsymbol{\nu} = 1 \pmod{2}, \quad (3)$$

we have $t(y) = t_0 \text{sgn}(y)$. Namely, when Eq. (3) is fulfilled, the chiral Majorana pair at the SC/magnetism domain experiences an additional mass domain due to the dislocation-induced lattice mismatch. This exactly resembles a 1D Jackiw-Rebbi problem and further results in a 0D MZM localized around the defect core, as shown in Fig. 1 (e), completing the final part of our nested domain wall construction for defect MBSs. Similar nested domains will simultaneously show up for the dislocation core at the bottom surface, as well as the other two corners of the cutting plane. This is how both Eq. (1) and Eq. (3) together serves as a sufficient topological condition for the emergence of defect MBSs.

B. Boundary Conditions & Majorana Inflation

Geometrically, a dislocation-induced cutting plane \mathcal{P}_c can terminate at either a crystal surface or another dislocation, leading to two seemingly different yet equivalent boundary conditions. For example, we can start from a dislocation dipole and move one dislocation towards the crystal side surface. This expands \mathcal{P}_c until the dislocation hits the side surface and further merges with it. This process is reversible and thus transforms the aforementioned boundary conditions from one to another.

In Fig. 2 (a), we schematically show the distributions of Majorana modes for the dislocation-dipole geometry. Each of the four dislocation cores will bind one MZM denoted by the quasiparticle operators $\gamma_i = \gamma_i^\dagger$ with $i \in \{1, 2, 3, 4\}$. In the cylindrical geometry shown in Fig. 2 (a), the chiral Majorana hinge modes always feature a finite-size gap that is inversely proportional to the cylinder radius [52], as shown in Fig. 2 (b). This gap is a manifestation of the anti-periodic boundary condition of 1D Majorana modes and can be removed by updating the boundary condition to a periodic one with a π -flux insertion. Thus, despite their chiral Majorana dispersions, the hinges do not carry any strictly *zero-energy mode* when they enclose a dislocation dipole.

Because of this finite-size hinge gap, when the defect MZM merges with the hinge Majorana modes as shown in Fig. 2 (c), its zero-energy nature remains. This is because a zero mode can only be spoiled while interacting with another zero mode. Numerically, we find that the defect MZM eventually merges with the 1D chiral hinge mode, making the hinge to harbor a *1D zero-energy state* at $k = 0$, as schematically shown in Fig. 2 (d). Therefore, the corner-localized 0D MZMs of ET_2 can be inflated to 1D zero modes by simply changing the terminations of the cutting plane \mathcal{P}_c . Notably, this inflation process is reversible, and one can similarly “condense” a 1D zero mode into a 0D dMBS by recovering the dislocation dipole.

C. Embedded Higher-Order Topology

The fact that dMBSs are “corner” Majorana modes of the cutting plane motivates us to define a higher-order topology [53–57] for the dislocation-spanned subsystem. In particular,

- an *embedded* n th-order topology (dubbed ET_n) is defined by the presence of $(d-n)$ -dimensional gapless boundary of a d -dimensional subsystem, which is further embedded in a D -dimensional bulk system with $D > d > n > 0$.

ET_n is thus a higher-order generalization of “embedded topology” proposed in Ref. [58, 59]. Our recipe for dMBSs features $D = 3$, $d = 2$ and $n = 2$, which thus corresponds to a class D ET_2 phase by definition.

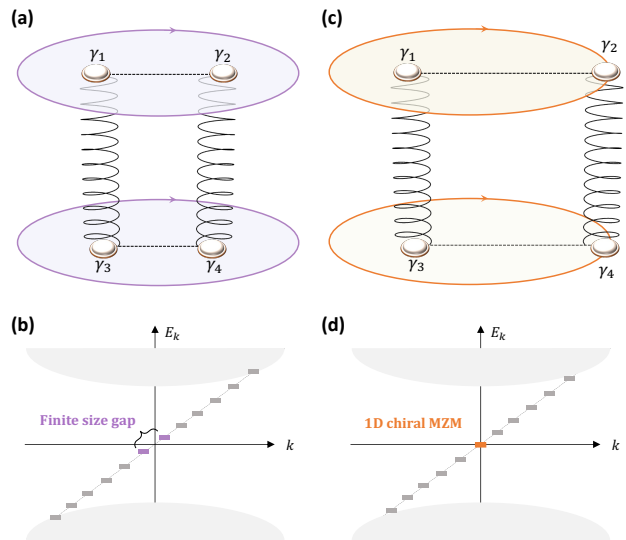


FIG. 2. “Inflation” of a Majorana mode from 0D to 1D. (a) shows a schematic of a dislocation dipole and their dMBSs. The surface Chern number enforces a pair of 1D chiral Majorana modes circulating around the top/bottom surface. The chiral Majorana modes yield a finite-size energy gap, as schematically shown in (b). When the cutting plane terminates at the sample boundary shown in (c), the defect MZMs $\gamma_{2,4}$ move to the hinges and merge with the chiral hinge modes, decorating each 1D chiral mode with a zero-energy state. Notably, the total number of zero-energy Majorana modes remains to be four while evolving from (a) to (c).

III. MODEL

In this section, we provide a minimal lattice model for $\text{FeTe}_{1-x}\text{Se}_x$ to demonstrate the above ET_2 recipe. Bulk superconductivity and surface ferromagnetism (FM) are also included in our model setup. By analyzing the competition of SC and FM for the Dirac surface states, we map out a surface topological phase diagram to discuss when Eq. (1) will be fulfilled. This can be directly translated to a condition for ET_2 to emerge in $\text{FeTe}_{1-x}\text{Se}_x$, which we verify through explicit screw dislocation simulations for our minimal model.

A. Hamiltonian

Our minimal Bogoliubov-de Gennes (BdG) Hamiltonian for $\text{FeTe}_{1-x}\text{Se}_x$ is

$$\mathcal{H}_{\text{BdG}}(\mathbf{k}) = \begin{pmatrix} \mathcal{H}_0(\mathbf{k}) - \mu & \Delta(\mathbf{k}) \\ \Delta^\dagger(\mathbf{k}) & -\mathcal{H}_0^*(-\mathbf{k}) + \mu \end{pmatrix}, \quad (4)$$

where the normal-state Hamiltonian $\mathcal{H}_0 = v(\sin k_y \Gamma_1 - \sin k_x \Gamma_2 + \sin k_z \Gamma_4) + m(\mathbf{k}) \Gamma_5$. The Γ matrices are $\Gamma_1 = \sigma_x \otimes s_x$, $\Gamma_2 = \sigma_x \otimes s_y$, $\Gamma_3 = \sigma_x \otimes s_z$, $\Gamma_4 = \sigma_y \otimes s_0$, $\Gamma_5 = \sigma_z \otimes s_0$, where $s_{0,x,y,z}$ and $\sigma_{0,x,y,z}$ are Pauli matrices for spin and orbital d.o.f., respectively. Here $m(\mathbf{k}) =$

$m_0 - m_1(\cos k_x + \cos k_y) - m_2 \cos k_z$ and μ is the chemical potential. We choose $v = 1$, $m_0 = -4$, $m_1 = -2$, $m_2 = 1$ to ensure a single topological band inversion at Z [60, 61], leading to $\nu_0 = 1$ and $\boldsymbol{\nu} = (0, 0, 1)$. This well matches the low-energy topological band ordering of $\text{FeTe}_{1-x}\text{Se}_x$. To introduce superconductivity, we adopt a spin-singlet extended s -wave pairing for our model, where the pairing matrix $\Delta(\mathbf{k}) = [\Delta_0 + \Delta_1(\cos k_x + \cos k_y)](i\sigma_0 \otimes s_y)$. Here Δ_0 (Δ_1) is the on-site (nearest-neighbor) intra-orbital pairing strength.

Finally, following the experimental observations of $\text{FeTe}_{1-x}\text{Se}_x$ in Ref. [45, 46, 48], we introduce uniform surface ferromagnetism to both top and bottom (001) surfaces in a finite-size slab geometry, with N_z layers stacked along \hat{z} direction. $\mathcal{H}_{\text{FM}} = f(z)[g_1\sigma_0 + g_2\sigma_z] \otimes (\mathbf{s} \cdot \mathbf{M})$ with $f(z) = \delta_{z,1} + \delta_{z,N_z}$ for a lattice layer index $z = 1, 2, \dots, N_z$. Here $\delta_{z,i}$ is the Kronecker delta function, \mathbf{M} denotes the surface magnetization, and $g_1 \pm g_2$ are the effective isotropic Landé g -factor for the two orbitals involved in our model. We take $g_1 = 0.5$ and $g_2 = 0.2$ in our numerical simulations throughout this work. More discussions on the experimental aspects of $\text{FeTe}_{1-x}\text{Se}_x$ and other candidate materials, can be found in Sec. V.

B. Surface Topological Phase Diagram: Condition for dMBSs & Partial Fermi Surface

The first step to realize dMBSs or class-D ET_2 is to identify the concrete condition to achieve Eq. (1) for our system by studying the competition between magnetism and superconductivity on the (001) surfaces. Note that the (001) Dirac surface state is localized around $\bar{\Gamma}$, the center of the surface Brillouin zone (BZ). As a result, the surface state will develop an *isotropic* pairing gap from the self-proximity effect [61], irrespective of the s_{\pm} nature of $\Delta(\mathbf{k})$. In fact, the s_{\pm} pairing will only play a role for ET_2 when the surface magnetism is absent (i.e., for symmetry class DIII), which will be discussed in Sec. IV. For the purpose of $\text{FeTe}_{1-x}\text{Se}_x$ and its class D ET_2 physics, we can simplify the pairing term to an on-site s -wave type by setting $\Delta_1 = 0$.

We further remark that the surface Dirac fermion has a continuous rotation symmetry around the z -axis in the low-energy limit. Therefore, the effect of a general FM configuration $\mathbf{M} = (M_x, M_y, M_z)$ is always equivalent to that of $\mathbf{M}' = (0, M_{\parallel}, M_z)$ up to a coordinate transformation, where $M_{\parallel} = \sqrt{M_x^2 + M_y^2}$. Without loss of generality, we thus consider $\mathbf{M} = (0, M_y, M_z)$, and the surface Hamiltonian reads,

$$\begin{aligned} \mathcal{H}_{\text{surf}} = & v_F(k_x\tau_zs_y - k_y\tau_0s_x) - \mu\tau_zs_0 \\ & + \Delta_0\tau_ys_y + \Sigma_y\tau_0s_y + \Sigma_z\tau_zs_z, \end{aligned} \quad (5)$$

where \mathbf{s} and $\boldsymbol{\tau}$ represent spin and particle-hole degree of freedom, respectively. v_F is the surface Fermi velocity. Up to the first-order perturbation approximation, $\Sigma_y \approx g_1M_y$ and $\Sigma_z \approx g_1M_z$ are the Zeeman en-

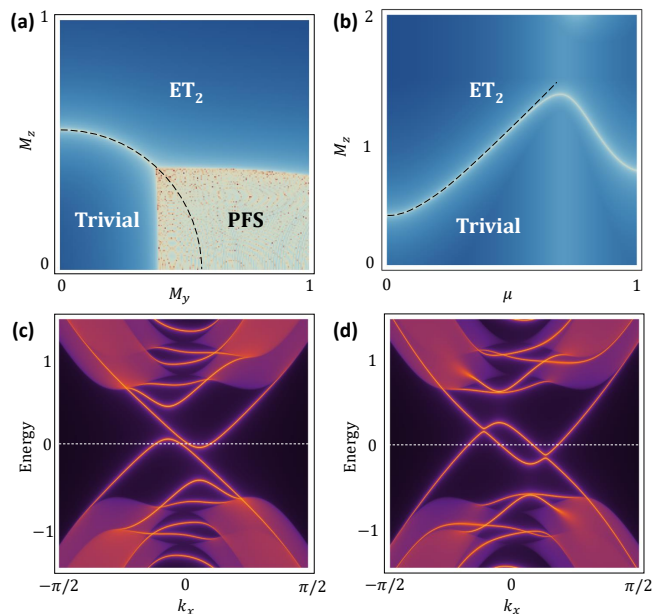


FIG. 3. Surface topological phase diagrams as a function of (M_y, M_z) and (M_z, μ) are shown in (a) and (b). The darker the blue color is, the larger the surface energy gap is. The region colored in white has no energy gap, and could indicate the existence of either a surface topological phase transition or a partial Fermi surface (PFS). Note that ET_2 and PFS can coexist. (c) shows the surface spectrum of a PFS along k_x with $(M_y, M_z) = (0.5, 0.05)$. An example of surface spectrum with coexisting ET_2 and PFS is shown in (d) with $(M_y, M_z) = (0.9, 0.05)$.

ergies [60]. Notably, condition of Eq. (1) is primarily concerned with the gap structures at $\bar{\Gamma}$. We thus find that $E_{\bar{\Gamma}} = \pm\sqrt{\mu^2 + \Delta_0^2} \pm \sqrt{\Sigma_y^2 + \Sigma_z^2}$. If we add back $\Sigma_x \approx g_1M_x$, then the surface gap closing condition is $\mu^2 + \Delta_0^2 = \boldsymbol{\Sigma}^2$ with $\boldsymbol{\Sigma} = (\Sigma_x, \Sigma_y, \Sigma_z)$. It is then easy to check that the ET_2 condition of Eq. (1) now becomes

$$|\boldsymbol{\Sigma}| > \sqrt{\mu^2 + \Delta_0^2}, \quad (6)$$

which coincides with the condition for the Dirac surface states to carry a BdG Chern number $|\mathcal{C}| = 1$. This non-trivial \mathcal{C} accounts for the chiral Majorana hinge modes in Fig. 1 (c), a crucial step to complete the nested domain wall configuration for achieving ET_2 . According to Eq. (3), a pair of screw or edge dislocations featuring an odd b_z will span a 2D cutting plane with class D ET_2 . Given the existence of such dislocations, Eq. (6) now serves as the ET_2 condition for $\text{FeTe}_{1-x}\text{Se}_x$.

On the other hand, a large in-plane \mathbf{M} is capable of inducing partial Fermi surface (PFS) in a superconducting TI [62, 63]. As shown in Fig. 3 (c) and (d), PFS occurs when some surface quasi-particle bands cross zero energy to form metal-like band patterns. While the formation of PFS is *irrelevant* to our target ET_2 physics, however, it can coexist with ET_2 and thus contributes an important part of our surface phase diagram. As

an intuitive example, we consider $\mathbf{M} = (0, M_y, 0)$ and find the dispersion of $\mathcal{H}_{\text{surf}}$ at $k_y = 0$ is $E_{\alpha\beta}(k_x) = \alpha\Sigma_y + \beta\sqrt{(v_F k_x - \alpha\mu)^2 + \Delta_0^2}$ with $\alpha, \beta = \pm$. For $\alpha\beta < 0$, $E_{\alpha\beta}$ has two zero-energy solutions at $k_x = k_\alpha^{(\pm)}$, with

$$k_\alpha^{(\pm)} = \frac{1}{v_F}(\alpha\mu \pm \sqrt{\Sigma_y^2 - \Delta_0^2}). \quad (7)$$

Therefore, when $|\Sigma_y| \geq |\Delta_0|$, $E_{+-} = 0$ and $E_{-+} = 0$ lead to four k_x solutions that form two sets of partial Fermi surfaces. Thanks to the rotation symmetry of Dirac surface Hamiltonian, we expect this PFS condition to be generalized to

$$|\Sigma_{\parallel}| \geq |\Delta_0| \quad \text{for } M_z = 0, \quad (8)$$

where $\Sigma_{\parallel} = g_1 M_{\parallel}$. Combining Eq. (6) with Eq. (8), we conclude that with $|M_z| \ll M_{\parallel}$, increasing M_{\parallel} will always first drive the formation of PFS ($M_{\parallel} \approx |\Delta_0|$) before ET₂ phase is achieved ($M_{\parallel} = \sqrt{\Delta_0^2 + \mu^2}$).

The above analytical results are in excellent agreement with our numerical surface topological phase diagram in Fig. 3 (a). This M_y - M_z phase diagram is essentially an energy-gap mapping of surface BdG spectrum for Eq. (4) in a thick slab geometry along \hat{z} direction, where we take $\mu = \Delta_0 = 0.2$. The color in this logarithmic plot is a measure of the energy gap of the lowest BdG band, and in particular, regions colored in white feature a vanishing BdG gap, i.e., either a topological phase transition or a PFS phase. Clearly, our analytical condition of ET₂ (black dashed line) in Eq. (6) matches perfectly with the numerical finding in Fig. 3 (a). In addition, Eq. (8) predicts a critical $M_y^{(c)} = \Sigma_{\parallel}^{(c)}/g_1 = \Delta_0/g_1 = 0.4$, also agreeing with numerically-mapped boundary of PFS phase at $M_z = 0$. As shown in Fig. 3 (a), PFS survives until M_z reaches a critical value of ~ 0.4 , and it is generally absent when $M_z > M_{\parallel}$. Importantly, PFS coexists with ET₂ most of the time in the phase diagram. So we expect that in a large M_{\parallel} system, *observation of PFS will serve as a promising indicator for ET₂ in the system.*

In Fig. 3 (b), we further study the effect of chemical potential μ on the formation of ET₂. For a small μ , the topological phase boundary separating ET₂ and trivial phase is well captured by the dashed guideline predicted by Eq. (6). Notably, the phase boundary undergoes a sudden turn at $\mu \sim 0.7$ and starts to deviate from the analytical results. This is because the bulk-band physics is getting more involved as μ grows, and thus our effective surface theory is no longer expected to faithfully describe the phase boundary of ET₂.

C. Numerical Simulation of dMBSs

To confirm the ET₂ phase, we consider to place our minimal model for $\text{FeTe}_{1-x}\text{Se}_x$ on a $28 \times 28 \times 28$ lattice. Periodic boundary conditions are considered for both x and y directions of the lattice cube to eliminate possible

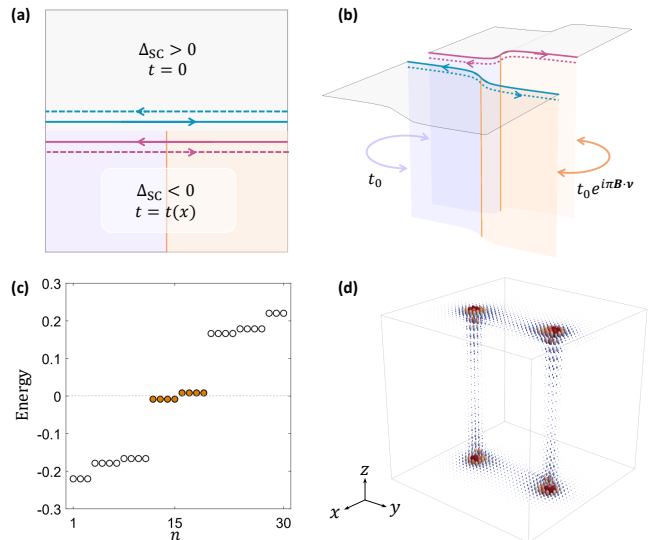


FIG. 4. Time-reversal-invariant ET₂ phase driven by an extended s -wave pairing with $(\Delta_0, \Delta_1) = (-0.85, 0.5)$. (a) and (b) illustrate a nested domain wall construction similar to that in Fig. 1. Two pairs of helical Majorana modes now show up, the gluing of which leads to a Kramers pair of Majorana bound states at each dislocation core. (c) shows the energy spectrum of a $36 \times 36 \times 20$ lattice with a dislocation dipole that supports eight Majorana zero modes. By plotting the spatial wavefunction distribution of these Majorana modes in (d), we numerically confirm that each dislocation core binds one Majorana Kramers pair.

unwanted hinge modes in our simulations. Out-of-plane FM are considered for both the top and bottom layers of the lattice cube, following \mathcal{H}_{FM} . We further decorate our lattice system with a pair of screw dislocations with a Burgers vector $\mathbf{b} = (0, 0, 1)$. The dislocation dipole spans a 2D cutting plane \mathcal{P}_c that is parallel to the y - z plane. In principle, one can consider a pair of edge dislocations instead, as long as their Burgers vectors satisfy

$$b_z \equiv 1 \pmod{2}. \quad (9)$$

As the FM is gradually turned on, the (001) surface gaps close and reopen in our cubic geometry following Fig. 3 (a), after which four zero-energy modes show up in the energy spectrum. In Fig. 1 (f), we visualize the spatial distribution of the zero-mode wavefunctions in the cubic geometry and find each of the four surface dislocation cores is trapping one of the zero modes. These dislocation-bound Majorana zero modes are exactly the defining boundary signature of ET₂ in our system.

IV. s_{\pm} -WAVE PAIRING & CLASS DIII ET₂

For tFeSC candidates such as $\text{FeTe}_{1-x}\text{Se}_x$ and LiFeAs , the bulk s_{\pm} pairing as described by $\Delta(\mathbf{k})$ is supported by experimental observations [64–66]. In particular, $\Delta_1 \neq 0$ is crucial for enabling a relative π -phase difference for

the local superconductivity orders of the Γ and M pockets. As we have discussed, in the above ET_2 recipe, it is the competition between SC and FM, rather than the explicit SC pairing type, that is crucial for enabling the dislocation Majorana bound states. In this section, we show that s_{\pm} pairing is *indeed* important for achieving a new class of time-reversal-invariant ET_2 in symmetry class DIII, but *only* when the surface FM is absent.

Our new recipe for class DIII ET_2 is motivated by the deep connection between hinge Majorana modes and ET_2 , as revealed in the nested domain wall picture. Even in the absence of surface FM, a bulk s_{\pm} pairing itself is capable of inducing a pairing mass domain for Dirac fermions living on the top (bottom) and side surfaces. As a result, the inter-surface hinge will harbor a pair of 1D helical Majorana modes that respect time-reversal symmetry [61]. As shown in Fig. 4, we can now follow a “cut and glue” procedure to reveal the dislocation physics. Similar to the steps we carried out in Sec. II, cutting the crystal now yields two pairs of helical Majorana modes trapped to the top hinges of the two smaller crystals [as shown in Fig. 4 (a) and (b)], as well as another two pairs bound to the bottom hinges. When gluing the crystal back together, a dislocation will introduce a π -phase domain to the inter-hinge binding term following Eq. (2), which will now trap a *Kramers pair* of Majorana zero modes around each of the surface dislocation core.

We now provide a lattice simulation to verify the existence of class DIII ET_2 with our minimal model of $FeTe_{1-x}Se_x$ in Eq. 4. We adopt the same model parameters of Fig. 1 (f), with no surface FM assumed and an additional update of $\Delta_0 = -0.85$ and $\Delta_1 = 0.5$ to emphasize the effect of s_{\pm} pairing. Note that the s_{\pm} condition for tFeSCs with $\Delta(\Gamma)\Delta(M) < 0$ is generally achieved when $|\Delta_0| < 2|\Delta_1|$. The energy spectrum for the system is calculated for a $36 \times 36 \times 20$ lattice geometry, with a pair of screw dislocations placed in the y - z plane. As shown in Fig. 4 (c), eight Majorana modes (orange circles) show up in the energy spectrum that are well separated from other higher-energy states. The small energy splitting for the Majorana modes is due to the finite-size effect of the cubic geometry. By plotting the Majorana wavefunctions in the real space, we find in Fig. 4 (d) that each surface dislocation core now harbors a pair of Majorana modes, which unambiguously demonstrates the existence of class DIII ET_2 trapped by the lattice dislocations.

V. MATERIAL CANDIDATES

In this section, we will discuss material candidates that can harbor ET_2 physics in both class D and class DIII. We will focus on the tFeSCs, especially $FeTe_{1-x}Se_x$ and LiFeAs, and further discuss their experimental relevance. However, ET_2 is not a privilege of tFeSCs and can in principle exist in other superconducting systems as well. We will discuss β -PdBi₂ as such an example.

A. $FeTe_{1-x}Se_x$

As highlighted in Sec. II and Sec. III, $FeTe_{1-x}Se_x$ naturally combines all necessary ingredients of our class D ET_2 recipe and manifests itself as perhaps the most promising platform for dMBSs. Thanks to the recent extensive experimental studies on both the normal-state topology and high-temperature superconductivity of $FeTe_{1-x}Se_x$ [29–31], we are capable of discussing its ET_2 possibility in a quantitative manner.

Evidence of surface magnetism in $FeTe_{1-x}Se_x$ has been experimentally established by a variety of measurement approaches. For example, an angle-resolved photoemission spectroscopy (ARPES) study in Ref. [45] reveals a direct surface gap of ~ 8 meV exactly at the surface Dirac point, in addition to the surface SC gap at the Fermi level. The spoiling of the Kramers degeneracy of Dirac surface state happens even above the superconducting transition temperature T_c , directly implying the breaking of time-reversal symmetry. Even though other more complex scenarios such as time-reversal-broken superconductivity is in principle possible [67, 68], a most straightforward interpretation of this magnetic gap would be the development of out-of-plane FM order on the surface. Similar evidence of surface FM has also been detected by the nanoscale quantum sensing of magnetic flux by nitrogen vacancy (NV) centers [46], where the magnetization is reported to feature an in-plane component as well.

Earlier experimental studies [30] further reveals a surface superconducting order of $\Delta_0 \sim 2$ meV and a chemical potential of $\mu \sim 4.4$ meV, in addition to $\Sigma_z \sim 4$ meV. Considering the condition in Eq. (6), ET_2 phase can be achieved with either (i) a slight electron doping to reduce μ , or (ii) an enhancement of surface FM. Notably, engineering surface FM could be more experimentally accessible. For example, neutron scattering measurements have revealed that a single interstitial Fe impurity can induce magnetic Friedel-like oscillation involving > 50 neighboring Fe sites [69]. As a result, an interstitial Fe impurity on the surface is capable of generating a local magnetic patch with $\Sigma_z \sim 10$ meV [70], which is large enough to enable ET_2 . Although interstitial Fe impurities could naturally exist during sample growth, they can also be deposited to the sample surface as adatoms [71]. This provides us a highly controlled approach to enhance surface FM of general tFeSCs.

Remarkably, for $FeTe_{1-x}Se_x$ films epitaxially grown with pulsed laser deposition (PLD), formation of screw dislocations can be feasibly controlled by simply tuning the deposition rate [44]. In particular, samples grown at a low deposition rate generally feature spiral-like surface morphology that encodes a screw dislocation with a Burgers vector of $\mathbf{b} = (0, 0, 1)$. This thus contributes the last key ingredient for materializing dMBSs in $FeTe_{1-x}Se_x$ at zero magnetic field.

Probe	Mag. Type	Orientation	Surf. Gap
ARPES	FM	\hat{z}	~ 8 meV
NV Center	FM	\hat{x} - \hat{z}	N/A

TABLE I. Summary of experiments on the surface magnetism in $\text{FeTe}_{1-x}\text{Se}_x$ with ARPES [45, 47] and NV center [46].

Materials	SCing Tc	\mathbb{Z}_2 Index	Bound State
$\text{FeTe}_{0.55}\text{Se}_{0.45}$	14.5 K	(1; 0,0,1)	MZM
LiFeAs	17 K	(1; 0,0,1)	MKP
(Li, Fe)OHFeSe	41 K	(1; 0,0,0)	N/A
β -PdBi ₂	5.3 K	(1; 0,0,1)	MZM

TABLE II. Candidate materials for ET_2 phases. Candidates with dislocation Majorana zero modes (MZMs) or Majorana Kramers pairs (MKPs) can realize an ET_2 of class D or DIII. (Li,Fe)OHFeSe is not expected to carry any ET_2 physics.

B. Other Fe-based Superconductors

Besides $\text{FeTe}_{1-x}\text{Se}_x$, evidences of Dirac surface states and vortex Majorana modes have also been found in other tFeSCs such as LiFeAs [26–28] and (Li,Fe)OHFeSe [25]. We first note that the topological band physics in (Li,Fe)OHFeSe is mainly attributed to the band inversion at Γ , thus leaving the system with zero weak indices. We therefore do not expect (Li,Fe)OHFeSe to carry ET_2 physics proposed in this work. A similar conclusion could be reached for $\text{CaKFe}_4\text{As}_4$, whose normal-state band inversion also happens at Γ due to a band folding effect [72].

The band structure of LiFeAs resembles that of $\text{FeTe}_{1-x}\text{Se}_x$ and features a weak-index vector $\boldsymbol{\nu} = (0, 0, 1)$. While we are not aware of any surface magnetism for LiFeAs, evidence of s_{\pm} pairing has been reported in earlier ARPES measurements [73]. This would make LiFeAs a good platform to host class DIII ET_2 and the associated defect Majorana Kramers pairs.

C. β -PdBi₂, Bismuth, and Beyond

Just like $\text{FeTe}_{1-x}\text{Se}_x$, β -PdBi₂ [49] features both a single band inversion at Z and *intrinsic* SC with a transition temperature of $T_c = 5.3$ K. By evaporating Cr atoms on Bi-terminated surface of β -PdBi₂, scanning tunneling microscopy (STM) technique can organize Cr atoms into a magnetic lattice that competes with SC on the surface [74]. In particular, both FM and anti-FM can be achieved by simply adjusting the lattice constant of the Cr adatoms. Therefore, we expect our ET_2 results on

$\text{FeTe}_{1-x}\text{Se}_x$ to be directly applicable to β -PdBi₂ as well.

ET_2 can also be achieved in an extrinsic manner by assembling all the necessary elements together in a heterostructure. For example, candidates of weak topological insulators carrying \mathbb{Z}_2 indices $(\nu_0; \nu_1, \nu_2, \nu_3) = (0; 0, 0, 1)$ have been experimentally established in a plethora of Bi-related materials, including BiTe [75], Bi₂TeI [76], Bi₄I₄ [77], and ZrTe₅ [78] etc. While these candidates are non-superconducting, one can design a ABC “trilayer” structure by growing a thin film of the above weak TIs on some superconducting substrates and further deposit another ferromagnetic layer on top. When a lattice screw dislocation with $\mathbf{b} = (0, 0, 1)$ occurs, the dMBSs should appear when Eq. (1) is satisfied.

We further note that a similar structure has been successfully fabricated for Bi(111) grown on a Nb(110) substrate, of which a ferromagnetic Fe cluster is placed on top [79]. Notably, the topological nature of Bi is disputable because of the tiny energy gap at L point, and Bi is believed to be either a higher-order topological insulator with trivial \mathbb{Z}_2 indices, or a strong topological insulator with $(\nu_0, \nu_1, \nu_2, \nu_3) = (1; 1, 1, 1)$. Interestingly, the latter scenario is recently supported by the observation of *helical electron modes bound to a screw dislocation* via an STM study [21]. These experimental progresses have together established Bi as another promising platform for dMBSs.

VI. EXPERIMENTAL DETECTION

Signatures of ET_2 for above material candidates can be feasibly revealed by mapping out the local density of states (LDOS) around lattice dislocations in experiments with the state-of-the-art STM technique. In this section, we numerically simulate the LDOS signals of dislocation-trapped Majorana modes for our minimal Hamiltonian in Eq. 4 using the iterative Green function method [80]. The geometry we considered involves an in-plane 20×40 lattice with a pair of screw dislocations embedded in the y - z plane, sitting symmetrically around the z -axis at $(x, y) = (10, 20)$. The spatial distance of the dislocations is denoted as δr_d . After sufficient iteration steps, the LDOS on the top (001) surface is $\mathcal{D}(\mathbf{r}, E) = -\frac{1}{\pi} \text{Im}[\mathcal{G}_{\text{surf}}(\mathbf{r}, E)]$, where $\mathcal{G}_{\text{surf}}(\mathbf{r}, E)$ is the surface Green function. This simulated LDOS signal can be directly compared with ultra-low-temperature STM data in future experiments.

When δr_d is much greater than the Majorana localization length $l_M \sim 3$, the hybridization between neighboring defect Majorana modes is negligible, as shown in Fig. 5 (a). We then expect each dislocation to carry a sharp LDOS peak at the zero bias, as numerically confirmed in Fig. 5 (b). Moving away from the dislocation core, the peak intensity gradually drops to zero without any further splitting, implying the existence of a single zero-energy mode. Meanwhile, we carry out a similar simulation with $\delta r_d \sim \mathcal{O}(l_M)$, where the dMBSs hybridize

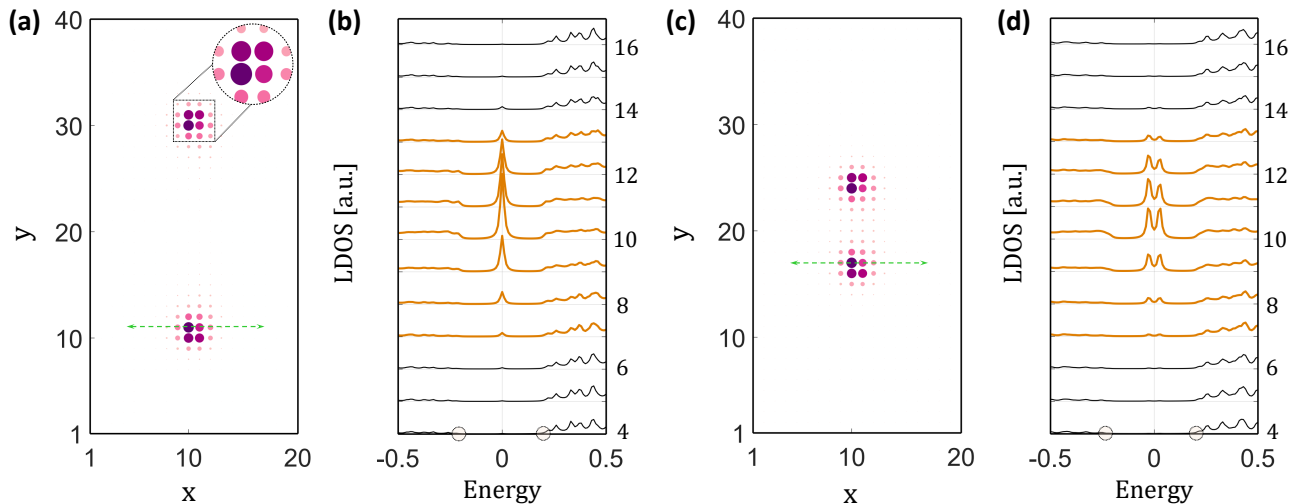


FIG. 5. Simulated surface LDOS patterns of dMBSs. (a) shows the zero-energy top surface LDOS of two dMBSs that are far away, with each dislocation core trapping a well-defined zero mode. The inset is a zoom-in plot around the dislocation core, which clearly shows the spatial anisotropy of the Majorana wavefunction. By doing a line cut across the dislocation following the green reference line, energy-dependent LDOS plots at each site is shown in (b), which shows a sharp zero-energy LDOS peak. The two circles on the horizontal axis indicate the position of the surface magnetic gap. When the two dislocations are brought together in (c), the zero-energy LDOS peak splits due to Majorana hybridizations, as shown in (d).

strongly [Fig. 5 (c)]. We similarly check the LDOS data near the bottom dislocation core and find the absence of any zero-bias peak in Fig. 5 (d). Instead, a double-peak structure emerges, indicating the annihilation of the dMBSs. As for $\text{FeTe}_{1-x}\text{Se}_x$, we expect l_M to be of the order of the superconducting coherence length $\xi_{SC} \sim 5$ nm, similar to that of vortex Majorana modes [22]. This sets a crucial length scale for δr_d , that only when $\delta r_d \gg \xi_{SC}$ will a clear experimental Majorana signal be expected.

We now remark on several phenomenological distinctions between defect and vortex Majorana modes. First, a quantum vortex always traps finite-energy Caroli-de Gennes-Matricorn (CdGM) states inside the SC gap, which can introduce Majorana-like signals near the zero energy and further complicates interpretations of experimental data. As for ET_2 , however, we do expect the dislocation core to carry fewer or even no subgap states besides the dMBS, as shown in our numerical simulations. This “cleanliness” of Majorana signal of ET_2 can significantly enhance the unambiguity of future experiments on relevant topics. In addition, while a vortex Majorana wavefunction is usually circular symmetric [11], our dMBS wavefunction is found to be anisotropic, since the screw dislocations explicitly break in-plane mirror symmetries of the lattice. This feature is clearly revealed in the surface LDOS plot of Fig. 5 (a), which should be accessible via STM measurements.

Because of the known inhomogeneity of $\text{FeTe}_{1-x}\text{Se}_x$ samples, it is likely that local magnetic and non-magnetic patches, instead of a uniform FM order, will appear on a real-world sample surface [47]. Nonetheless, our prediction of dMBSs still holds once the dislocation core overlaps with the FM patch, which can be feasibly as-

sembled by moving Fe adatoms. We further notice that applying a \hat{z} -directional magnetic field can facilitates the creation of ET_2 phase by enhancing the magnetic gap, at the price of introducing additional SC vortex physics. While our dMBS is immune to an applied magnetic field, Ref. [70] predicts that the field-induced SC vortices living inside the magnetic patch do *not* harbor any vortex Majorana modes, and are thus dubbed “empty vortices”. With such an external magnetic field, we thus expect the dMBS to contribute the *only* zero-bias peak signal to a STM scanning inside a local FM patch, and it will be further surrounded by a set of “satellite” empty vortices with no Majorana signal. This unique phenomenon, if being observed, will serve as a rather compelling experimental evidence for ET_2 .

VII. CONCLUSIONS AND DISCUSSIONS

We have proposed a new magnetic-field-free mechanism to trap non-Abelian Majorana zero modes with lattice dislocations, and further establish topological iron-based superconductors such as $\text{FeTe}_{1-x}\text{Se}_x$ as an ideal venue to realize dMBSs. This exotic defect Majorana physics manifests as an exemplar of an embedded higher-order topology, paving the way for exploring emergent subsystem topological physics. Notably, our recipe for dMBS is beyond tFeSCs and it further provides theoretical guidance to experimentally design and achieve dMBSs in other weak-index-carrying material systems such as β - PdBi_2 . Given the remarkable capabilities of manipulating both the screw dislocations and surface magnetism in $\text{FeTe}_{1-x}\text{Se}_x$ that have been reported in the literature, we

believe that our proposal of dislocation Majorana physics will soon be experimentally realizable.

We further note that the ET_2 uncovered in this work is “extrinsic”, in the sense that the dMBS cannot be characterized by a 2D bulk topological invariant of the subsystem. An interesting future direction is to explore the possibility of crystalline-symmetry-protected “intrinsic” ET_2 . While a screw dislocation necessarily breaks the majority types of lattice symmetries, edge dislocations or even partial dislocations are probably better geometric subsystems to consider for this purpose [81]. Meanwhile, a generalization of ET_2 to nonsuperconducting systems should also be straightforward, and we do expect an ET_2 phase in class AIII or BDI to carry fractionally-charged zero modes that are stabilized by chiral symmetry.

Finally, motivated by the recent theoretical proposal of boundary-obstructed topological phases [82, 83], we conjecture the existence of *defect-obstructed topological phase* (DOTP) as a new class of topological matter. Namely, two phases that are both bulk and boundary topological equivalent can be *defect obstructed*, if the subsystem energy gap of a lattice or order-parameter defect must close while connecting the two phases. For example, the vortex topological phase transition of a doped *s*-wave superconducting TI described in Ref. [14] could separate

two phases that are defect (i.e., vortex) obstructed. Both phases, living before and after the vortex transition, are bulk topologically trivial. However, a topological vortex phase does feature a different 1D BdG Wannier orbital configuration from that of a trivial phase, a feature that is revealed only when a 1D vortex line is inserted in the bulk system. Apparently, the DOTP is deeply connected to the embedded (higher-order) topological physics. We believe that a description of DOTP based on the topological quantum chemistry language is necessary to advance our understanding of subsystem topologies and will possibly lead us to a novel simple mathematical diagnostic approach for both ET and ET_2 . We will leave this interesting direction to future works.

ACKNOWLEDGMENTS

We thank X. Liu, C.-Z. Chen, X.-Q. Sun, and J. Yu for helpful discussions. We are particularly indebted to L.-Y. Kong and X. Wu for the inspiring discussions on the candidate materials. This work is supported by a start-up funding at the University of Tennessee.

-
- [1] R. Jackiw and C. Rebbi, *Phys. Rev. D* **13**, 3398 (1976).
 - [2] W. P. Su, J. R. Schrieffer, and A. J. Heeger, *Phys. Rev. Lett.* **42**, 1698 (1979).
 - [3] Y. Ran, Y. Zhang, and A. Vishwanath, *Nature Physics* **5**, 298 (2009).
 - [4] G. Rosenberg, H.-M. Guo, and M. Franz, *Phys. Rev. B* **82**, 041104 (2010).
 - [5] V. Juričić, A. Mesaros, R.-J. Slager, and J. Zaanen, *Phys. Rev. Lett.* **108**, 106403 (2012).
 - [6] R.-J. Slager, A. Mesaros, V. Juričić, and J. Zaanen, *Phys. Rev. B* **90**, 241403 (2014).
 - [7] B. Roy and V. Juričić, *Phys. Rev. Research* **3**, 033107 (2021).
 - [8] N. Read and D. Green, *Phys. Rev. B* **61**, 10267 (2000).
 - [9] A. Y. Kitaev, *Physics-Uspekhi* **44**, 131 (2001).
 - [10] D. A. Ivanov, *Phys. Rev. Lett.* **86**, 268 (2001).
 - [11] L. Fu and C. L. Kane, *Phys. Rev. Lett.* **100**, 096407 (2008).
 - [12] R. M. Lutchyn, J. D. Sau, and S. Das Sarma, *Phys. Rev. Lett.* **105**, 077001 (2010).
 - [13] J. D. Sau, R. M. Lutchyn, S. Tewari, and S. Das Sarma, *Phys. Rev. Lett.* **104**, 040502 (2010).
 - [14] P. Hosur, P. Ghaemi, R. S. K. Mong, and A. Vishwanath, *Phys. Rev. Lett.* **107**, 097001 (2011).
 - [15] D. Asahi and N. Nagaosa, *Phys. Rev. B* **86**, 100504 (2012).
 - [16] J. C. Y. Teo and T. L. Hughes, *Phys. Rev. Lett.* **111**, 047006 (2013).
 - [17] T. L. Hughes, H. Yao, and X.-L. Qi, *Phys. Rev. B* **90**, 235123 (2014).
 - [18] K.-I. Imura and Y. Takane, *Phys. Rev. B* **84**, 245415 (2011).
 - [19] R.-X. Zhang and C.-X. Liu, *Phys. Rev. Lett.* **120**, 156802 (2018).
 - [20] H. Hamasaki, Y. Tokumoto, and K. Edagawa, *Applied Physics Letters* **110**, 092105 (2017).
 - [21] A. K. Nayak, J. Reiner, R. Queiroz, H. Fu, C. Shekhar, B. Yan, C. Felser, N. Avraham, and H. Beidenkopf, *Science advances* **5**, eaax6996 (2019).
 - [22] D. Wang, L. Kong, P. Fan, H. Chen, S. Zhu, W. Liu, L. Cao, Y. Sun, S. Du, J. Schneeloch, *et al.*, *Science* **362**, 333 (2018).
 - [23] L. Kong, S. Zhu, M. Papaj, H. Chen, L. Cao, H. Isobe, Y. Xing, W. Liu, D. Wang, P. Fan, *et al.*, *Nature Physics* **15**, 1181 (2019).
 - [24] S. Zhu, L. Kong, L. Cao, H. Chen, M. Papaj, S. Du, Y. Xing, W. Liu, D. Wang, C. Shen, *et al.*, *Science* **367**, 189 (2020).
 - [25] Q. Liu, C. Chen, T. Zhang, R. Peng, Y.-J. Yan, C.-H.-P. Wen, X. Lou, Y.-L. Huang, J.-P. Tian, X.-L. Dong, G.-W. Wang, W.-C. Bao, Q.-H. Wang, Z.-P. Yin, Z.-X. Zhao, and D.-L. Feng, *Phys. Rev. X* **8**, 041056 (2018).
 - [26] L. Cao, W. Liu, G. Li, G. Dai, Q. Zheng, Y. Wang, K. Jiang, S. Zhu, L. Huang, L. Kong, F. Yang, X. Wang, W. Zhou, X. Lin, J. Hu, C. Jin, H. Ding, and H.-J. Gao, *Nature Communications* **12** (2021).
 - [27] W. Liu, Q. Hu, X. Wang, Y. Zhong, F. Yang, L. Kong, L. Cao, G. Li, K. Okazaki, T. Kondo, *et al.*, *arXiv preprint arXiv:2111.03786* (2021).
 - [28] M. Li, G. Li, L. Cao, X. Zhou, X. Wang, C. Jin, C.-K. Chiu, S. J. Pennycook, Z. Wang, and H.-J. Gao, *Nature* **606**, 890 (2022).
 - [29] Z. Wang, P. Zhang, G. Xu, L. K. Zeng, H. Miao, X. Xu, T. Qian, H. Weng, P. Richard, A. V. Fedorov, H. Ding,

- X. Dai, and Z. Fang, *Phys. Rev. B* **92**, 115119 (2015).
- [30] P. Zhang, K. Yaji, T. Hashimoto, Y. Ota, T. Kondo, K. Okazaki, Z. Wang, J. Wen, G. D. Gu, H. Ding, and S. Shin, *Science* **360**, 182 (2018).
- [31] P. Zhang, Z. Wang, X. Wu, K. Yaji, Y. Ishida, Y. Kohama, G. Dai, Y. Sun, C. Bareille, K. Kuroda, T. Kondo, K. Okazaki, K. Kindo, X. Wang, C. Jin, J. Hu, R. Thomale, K. Sumida, S. Wu, K. Miyamoto, T. Okuda, H. Ding, G. D. Gu, T. Tamegai, T. Kawakami, M. Sato, and S. Shin, *Nature Physics* **15**, 41 (2018).
- [32] C. Chen, K. Jiang, Y. Zhang, C. Liu, Y. Liu, Z. Wang, and J. Wang, *Nature Physics* **16**, 536 (2020).
- [33] J.-X. Yin, Z. Wu, J. Wang, Z. Ye, J. Gong, X. Hou, L. Shan, A. Li, X. Liang, X. Wu, *et al.*, *Nature Physics* **11**, 543 (2015).
- [34] S. S. Zhang, J.-X. Yin, G. Dai, L. Zhao, T.-R. Chang, N. Shumiya, K. Jiang, H. Zheng, G. Bian, D. Multer, M. Litskevich, G. Chang, I. Belopolski, T. A. Cochran, X. Wu, D. Wu, J. Luo, G. Chen, H. Lin, F.-C. Chou, X. Wang, C. Jin, R. Sankar, Z. Wang, and M. Z. Hasan, *Phys. Rev. B* **101**, 100507 (2020).
- [35] L. Fu, C. L. Kane, and E. J. Mele, *Phys. Rev. Lett.* **98**, 106803 (2007).
- [36] G. Xu, B. Lian, P. Tang, X.-L. Qi, and S.-C. Zhang, *Phys. Rev. Lett.* **117**, 047001 (2016).
- [37] L.-H. Hu, X. Wu, C.-X. Liu, and R.-X. Zhang, *arXiv preprint arXiv:2110.11357* (2021).
- [38] K. Jiang, X. Dai, and Z. Wang, *Phys. Rev. X* **9**, 011033 (2019).
- [39] Y. Zhang, K. Jiang, F. Zhang, J. Wang, and Z. Wang, *Phys. Rev. X* **11**, 011041 (2021).
- [40] X. Wu, J.-X. Yin, C.-X. Liu, and J. Hu, *arXiv preprint arXiv:2004.05848* (2020).
- [41] R. Song, P. Zhang, and N. Hao, *Phys. Rev. Lett.* **128**, 016402 (2022).
- [42] C.-K. Chiu and Z. Wang, *Phys. Rev. Lett.* **128**, 237001 (2022).
- [43] A. Ghazaryan, A. Kirmani, R. M. Fernandes, and P. Ghaemi, *arXiv preprint arXiv:2207.12425* (2022).
- [44] A. Gerbi, R. Buzio, E. Bellingeri, S. Kawale, D. Marrè, A. S. Siri, A. Palenzona, and C. Ferdeghini, *Superconductor Science and Technology* **25**, 012001 (2011).
- [45] N. Zaki, G. Gu, A. Tsvelik, C. Wu, and P. D. Johnson, *Proceedings of the National Academy of Sciences* **118** (2021).
- [46] N. J. McLaughlin, H. Wang, M. Huang, E. Lee-Wong, L. Hu, H. Lu, G. Q. Yan, G. Gu, C. Wu, Y.-Z. You, and C. R. Du, *Nano Letters* **21**, 7277 (2021).
- [47] Y. Li, N. Zaki, V. O. Garlea, A. T. Savici, D. Fobes, Z. Xu, F. Camino, C. Petrovic, G. Gu, P. D. Johnson, J. M. Tranquada, and I. A. Zaliznyak, *Nature Materials* **20**, 1221 (2021).
- [48] C. Farhang, N. Zaki, J. Wang, G. Gu, P. D. Johnson, and J. Xia, *arXiv preprint arXiv:2208.06905* (2022).
- [49] M. Sakano, K. Okawa, M. Kanou, H. Sanjo, T. Okuda, T. Sasagawa, and K. Ishizaka, *Nature Communications* **6** (2015).
- [50] L. Fu and C. L. Kane, *Phys. Rev. Lett.* **102**, 216403 (2009).
- [51] A. R. Akhmerov, J. Nilsson, and C. W. J. Beenakker, *Phys. Rev. Lett.* **102**, 216404 (2009).
- [52] J. Alicea, *Reports on progress in physics* **75**, 076501 (2012).
- [53] W. A. Benalcazar, B. A. Bernevig, and T. L. Hughes, *Science* **357**, 61 (2017).
- [54] W. A. Benalcazar, B. A. Bernevig, and T. L. Hughes, *Phys. Rev. B* **96**, 245115 (2017).
- [55] F. Schindler, A. M. Cook, M. G. Vergniory, Z. Wang, S. S. Parkin, B. A. Bernevig, and T. Neupert, *Science advances* **4**, eaat0346 (2018).
- [56] F. Schindler, Z. Wang, M. G. Vergniory, A. M. Cook, A. Murani, S. Sengupta, A. Y. Kasumov, R. Deblock, S. Jeon, I. Drozdov, *et al.*, *Nature physics* **14**, 918 (2018).
- [57] R.-X. Zhang, F. Wu, and S. Das Sarma, *Phys. Rev. Lett.* **124**, 136407 (2020).
- [58] T. I. Tügel, V. Chua, and T. L. Hughes, *Phys. Rev. B* **100**, 115126 (2019).
- [59] S. Velury and T. L. Hughes, *Phys. Rev. B* **105**, 184105 (2022).
- [60] C.-X. Liu, X.-L. Qi, H. Zhang, X. Dai, Z. Fang, and S.-C. Zhang, *Phys. Rev. B* **82**, 045122 (2010).
- [61] R.-X. Zhang, W. S. Cole, and S. Das Sarma, *Phys. Rev. Lett.* **122**, 187001 (2019).
- [62] N. F. Q. Yuan and L. Fu, *Phys. Rev. B* **97**, 115139 (2018).
- [63] Z. Zhu, M. Papaj, X.-A. Nie, H.-K. Xu, Y.-S. Gu, X. Yang, D. Guan, S. Wang, Y. Li, C. Liu, J. Luo, Z.-A. Xu, H. Zheng, L. Fu, and J.-F. Jia, *Science* **374**, 1381 (2021).
- [64] T. Hanaguri, S. Niitaka, K. Kuroki, and H. Takagi, *Science* **328**, 474 (2010).
- [65] P. J. Hirschfeld, M. M. Korshunov, and I. I. Mazin, *Reports on Progress in Physics* **74**, 124508 (2011).
- [66] A. Chubukov, *Annual Review of Condensed Matter Physics* **3**, 57 (2012).
- [67] L.-H. Hu, P. D. Johnson, and C. Wu, *Phys. Rev. Research* **2**, 022021 (2020).
- [68] J. L. Lado and M. Sigrist, *Phys. Rev. Research* **1**, 033107 (2019).
- [69] V. Thampy, J. Kang, J. A. Rodriguez-Rivera, W. Bao, A. T. Savici, J. Hu, T. J. Liu, B. Qian, D. Fobes, Z. Q. Mao, C. B. Fu, W. C. Chen, Q. Ye, R. W. Erwin, T. R. Gentile, Z. Tesanovic, and C. Broholm, *Phys. Rev. Lett.* **108**, 107002 (2012).
- [70] X. Wu, S. B. Chung, C. Liu, and E.-A. Kim, *Phys. Rev. Research* **3**, 013066 (2021).
- [71] P. Fan, F. Yang, G. Qian, H. Chen, Y.-Y. Zhang, G. Li, Z. Huang, Y. Xing, L. Kong, W. Liu, *et al.*, *Nature communications* **12**, 1 (2021).
- [72] W. Liu, L. Cao, S. Zhu, L. Kong, G. Wang, M. Papaj, P. Zhang, Y.-B. Liu, H. Chen, G. Li, *et al.*, *Nature communications* **11**, 1 (2020).
- [73] K. Umezawa, Y. Li, H. Miao, K. Nakayama, Z.-H. Liu, P. Richard, T. Sato, J. B. He, D.-M. Wang, G. F. Chen, H. Ding, T. Takahashi, and S.-C. Wang, *Phys. Rev. Lett.* **108**, 037002 (2012).
- [74] D.-J. Choi, C. G. Fernández, E. Herrera, C. Rubio-Verdú, M. M. Ugeda, I. Guillamón, H. Suderow, J. I. Pascual, and N. Lorente, *Phys. Rev. Lett.* **120**, 167001 (2018).
- [75] M. Eschbach, M. Lanius, C. Niu, E. Młyńczak, P. Gospodarič, J. Kellner, P. Schüffelgen, M. Gehlmann, S. Döring, E. Neumann, *et al.*, *Nature communications* **8**, 1 (2017).
- [76] N. Avraham, A. K. Nayak, A. Steinbok, A. Norris, H. Fu, Y. Sun, Y. Qi, L. Pan, A. Isaeva, A. Zeugner, C. Felser, B. Yan, and H. Beidenkopf, *Nature Materials* **19**, 610 (2020).
- [77] R. Noguchi, T. Takahashi, K. Kuroda, M. Ochi, T. Shira-sawa, M. Sakano, C. Bareille, M. Nakayama, M. Watson,

- K. Yaji, et al., *Nature* **566**, 518 (2019).
- [78] P. Zhang, R. Noguchi, K. Kuroda, C. Lin, K. Kawaguchi, K. Yaji, A. Harasawa, M. Lippmaa, S. Nie, H. Weng, et al., *Nature communications* **12**, 1 (2021).
- [79] B. Jäck, Y. Xie, J. Li, S. Jeon, B. A. Bernevig, and A. Yazdani, *Science* **364**, 1255 (2019).
- [80] M. L. Sancho, J. L. Sancho, J. L. Sancho, and J. Rubio, *Journal of Physics F: Metal Physics* **15**, 851 (1985).
- [81] A. Burleson, L.-H. Hu, and R.-X. Zhang, to appear soon.
- [82] E. Khalaf, W. A. Benalcazar, T. L. Hughes, and R. Queiroz, *Physical Review Research* **3**, 013239 (2021).
- [83] X. Wu, W. A. Benalcazar, Y. Li, R. Thomale, C.-X. Liu, and J. Hu, *Physical Review X* **10**, 041014 (2020).